

Journal of Materials Chemistry A

Accepted Manuscript



This is an *Accepted Manuscript*, which has been through the Royal Society of Chemistry peer review process and has been accepted for publication.

Accepted Manuscripts are published online shortly after acceptance, before technical editing, formatting and proof reading. Using this free service, authors can make their results available to the community, in citable form, before we publish the edited article. We will replace this *Accepted Manuscript* with the edited and formatted *Advance Article* as soon as it is available.

You can find more information about *Accepted Manuscripts* in the [Information for Authors](#).

Please note that technical editing may introduce minor changes to the text and/or graphics, which may alter content. The journal's standard [Terms & Conditions](#) and the [Ethical guidelines](#) still apply. In no event shall the Royal Society of Chemistry be held responsible for any errors or omissions in this *Accepted Manuscript* or any consequences arising from the use of any information it contains.

ARTICLE

In situ Fe K-edge X-Ray Absorption Spectroscopy study during cycling of $\text{Li}_2\text{FeSiO}_4$ and $\text{Li}_{2.2}\text{Fe}_{0.9}\text{SiO}_4$ Li ion battery materials

Cite this: DOI: 10.1039/x0xx00000x

Received 00th January 2012,
Accepted 00th January 2012

DOI: 10.1039/x0xx00000x

www.rsc.org/

Alexander W. Brownrigg^{a,b,e}, Gavin Mountjoy^a, Alan V. Chadwick^a, Maria Alfredsson^{a†}, Wim Bras^b, Juliette Billaud^c, A. Robert Armstrong^c, Peter G. Bruce^c, Robert Dominko^d, and Erik M. Kelder^e

In situ X-Ray Absorption Spectroscopy (XAS) results are presented for $\text{Li}_2\text{FeSiO}_4$ and $\text{Li}_{2.2}\text{Fe}_{0.9}\text{SiO}_4$, promising cathode materials for lithium-ion batteries. The aims are to establish the valence and local structure of Fe during charge and discharge to understand if the $\text{Fe}^{3+}/\text{Fe}^{4+}$ redox pair can be reached in the current battery design. It is found that the valence state changes between Fe^{+2} and Fe^{+3} , with no evidence of Fe^{+4} before the onset of electrolyte degradation. There is a reversible contraction and extension of the Fe-O bond lengths during cycling while the Fe-Si distance remains constant, which underlines the stability of the $\text{Li}_2\text{FeSiO}_4$ material. The same observations apply to $\text{Li}_{2.2}\text{Fe}_{0.9}\text{SiO}_4$ cathode material indicating that changing the stoichiometry does not provide any additional structural stability.

Introduction

Progress in the development of Li ion battery cathode materials is based upon the interplay of several defining features driven by the requirements of consumer markets. The materials should conform to criteria associated with energy density, cyclability, safety, and cost to ensure their future use in widespread energy storage applications.¹⁻³ The focus of electrochemical and structural characterization studies has been extended from robust layered intercalation oxides, such as, LiCoO_2 and LiMn_2O_4 to polyoxyanion materials with tetrahedral structural units.⁴

The quest for a suitable cathode material has included a focus on lithium iron silicates, which offer many benefits as prospective cathode materials while their complex polymorphism also makes them interesting from a fundamental perspective of solid state chemistry.⁵ Using abundant elements, like iron and silicon, offer an economic alternative to the Co based system. Safety is a driving factor in battery development and the Si-O bond provides stability similar to the P-O bond in LiFePO_4 compounds.⁴

Another advantage of the iron silicates, is the theoretical possibility to remove two Li ions from $\text{Li}_2\text{FeSiO}_4$, by utilizing the $\text{Fe}^{+2}/\text{Fe}^{+3}$ and the $\text{Fe}^{+3}/\text{Fe}^{+4}$ redox couples, thus, producing a higher capacity than 166 mAhg^{-1} for one Li ion. Although capacities greater than 200 mAhg^{-1} have been reported by several groups⁶⁻⁸ it has yet

to be clarified whether it was due to Fe^{+4} formation or electrolyte degradation.⁴

$\text{Li}_2\text{FeSiO}_4$ has been intensively studied and the crystal structures have been deduced in the *pristine* ($\text{Li}_2\text{FeSiO}_4$), *delithiated* (LiFeSiO_4) and *cycled* ($\text{Li}_2\text{FeSiO}_4$) states, using X-ray diffraction (XRD) and neutron diffraction measurements.^{5,9-13} Furthermore, the structural properties of various polymorphs have been investigated using computer modeling, including density functional theory (DFT) calculations to explore relationships between the macroscopic electrochemical properties and atomic structures.^{6,14-21} In particular, the geometry of FeO_4 tetrahedra in terms of orientation, size and distortion is thought to influence the equilibrium potential measured in the different polymorphs. As a result the equilibrium potential in the first cycle of the material differs from subsequent cycles, corresponding to an irreversible change in the structure during the first cycle.^{13,22}

The *pristine* material, $\gamma\text{-Li}_2\text{FeSiO}_4$, is prepared at temperatures between 600°C and 700°C and has a $\text{P2}_1/\text{n}$ space-group. This structure is characterized by edge sharing LiO_4 and FeO_4 tetrahedra, as well as LiO_4 tetrahedra, of which half are pointing in opposite directions.²³ The *delithiated* material, *inverse* $\beta\text{-Li}_2\text{FeSiO}_4$ with space-group $\text{Pmn}2_1$, shows corner linked tetrahedra with all species pointing along the *c* axis. In this structure the SiO_4 tetrahedra are isolated from each other, sharing corners with LiO_4 and (disordered) $(\text{Li/Fe})\text{O}_4$ tetrahedra. The *cycled* structure, $\beta\text{-Li}_2\text{FeSiO}_4$, also

crystallise in the $Pmn2_1$ space-group. As for the delithiated material all tetrahedra are pointing in the same direction, sharing only corners with each other. Along the a axis there are chains of $(\text{Li}/\text{Fe})\text{O}_4$ parallel to chains of alternating (ordered) LiO_4 and SiO_4 tetrahedra.¹⁴

X-ray Absorption Spectroscopy (XAS) is an experimental probe sensitive to changes in the valence and local structure of Fe sites, which can be used to address the questions regarding access to the $\text{Fe}^{3+}/\text{Fe}^{4+}$ redox couple, as well as the structural stability. There have only been two previous *in-situ* XAS studies of $\text{Li}_2\text{FeSiO}_4$ during cycling. The first study reported EXAFS analysis of only the first Fe-O shell.²⁴ The second one reported only Fe XANES results.⁶

For the purposes of this study, the focus will be placed on the γ (*pristine*), *inverse β* (*delithiated*) and the β (*cycled*) polymorphs of $\text{Li}_2\text{FeSiO}_4$, probing changes in the local atomic structure with respect to crystalline order. Establishing how the local structure of Fe changes upon charge and discharge, especially during the first cycle, is essential for tailoring the next generation of cathode materials to have the desired electrochemical characteristics. This is achieved by using *in situ* EXAFS to monitor the length of the Fe–O bond and longer distance correlations during cycling. By using two samples with different Li and Fe contents in the series $\text{Li}_{2+2a}\text{Fe}_{1-a}\text{SiO}_4$, *i.e.* $\text{Li}_2\text{FeSiO}_4$ and $\text{Li}_{2.2}\text{Fe}_{0.9}\text{SiO}_4$, we investigate the extent to which the structural changes during cycling can accommodate variations in stoichiometry.

In order to address the issue regarding the $\text{Fe}^{3+}/\text{Fe}^{4+}$ redox couple, *in situ* XANES has been undertaken to estimate the formal valence of the Fe atoms as Li is removed and inserted into the structure during battery cycling.

Experimental

Sample preparation

Stoichiometric amounts of Li acetate dehydrate (Acros), Fe (II) acetate and tetraethyl orthosilicate were mixed in ethanol with 2mL of acetic acid. After stirring, the suspension was transferred to a Teflon-lined autoclave and heated to 130°C for 12 hours. The resulting gel was dried under vacuum at 80°C, mixed with sucrose and ball milled under acetone for 30 minutes. Following acetone evaporation, the sample was annealed under flowing nitrogen at 600°C for 10 hours. The materials were then transferred to an Argon filled glove box (oxygen and water levels < 1ppm).

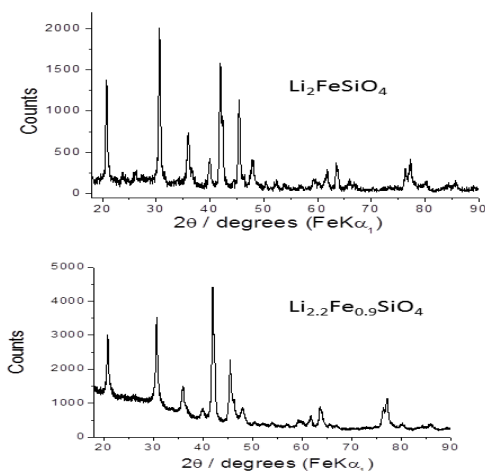
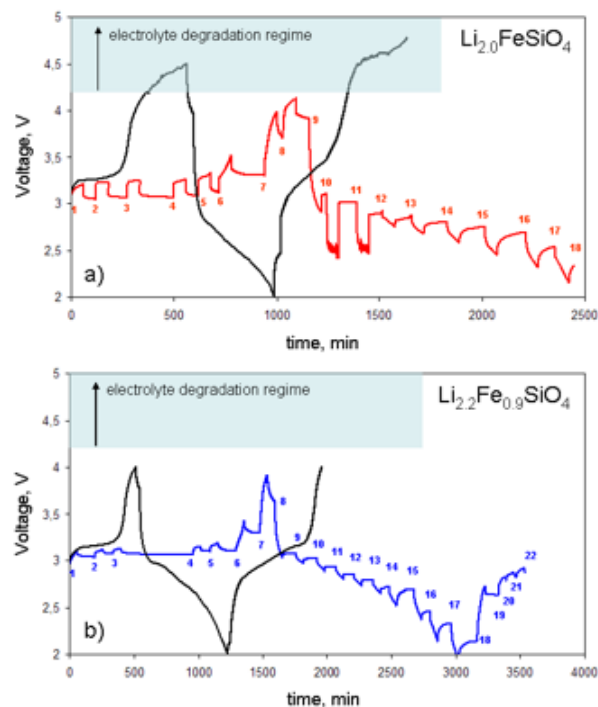


Figure 1. Powder X-ray diffraction pattern for pristine a) $\text{Li}_2\text{FeSiO}_4$ and b) $\text{Li}_{2.2}\text{Fe}_{0.9}\text{SiO}_4$

Sample characterisation

Power X-ray diffraction data were collected on a STOE STADIP diffractometer operating in transmission mode with $\text{Fe K}\alpha$ radiation ($\lambda = 1.936 \text{ \AA}$) to eliminate Fe fluorescence.^{5,8,25-29}

X-ray diffraction shows the samples to be highly pure (Figure 1). The $\text{Li}_2\text{FeSiO}_4$ sample is judged to contain approximately 2% impurities probably in the form of Li_2SiO_3 and $\text{Fe}_{(1-x)}\text{O}$. The Li_2SiO_3 is expected to be inactive during lithiation/delithiation. The $\text{Fe}_{(1-x)}\text{O}$ is only expected to be active at low voltages (conversion reactions) and this was not seen in our electrochemical measurements. The $\text{Li}_{2.2}\text{Fe}_{0.9}\text{SiO}_4$ sample is judged to be highly pure with negligible impurities. Note however that the diffraction patterns are not highly



sensitive to the Li/Fe ratio.

Figure 2. Electrochemical measurements of a) $\text{Li}_2\text{FeSiO}_4$ and b) $\text{Li}_{2.2}\text{Fe}_{0.9}\text{SiO}_4$. The black curves refer to galvanostatic charging and discharging of $1/2$ cycle, whereas the colored curves show the data of the cells used for the *in-situ* XAS experiments. The labels mentioned here are used for referring to the XAS data shown in the other figures.

Electrochemical measurements

Composite electrodes were prepared by ball-milling the active silicate material together with 8wt% of acetylene black and 10 wt% of EPDM in *n*-hexane. The obtained slurry was pressed on Al mesh and subsequently dried on Al discs having a typical mass of active material of 10–15mg/cm². Prior to use, the electrodes were further allowed to dry at 90°C in vacuum overnight. The *in situ* coffee bag-type cells consisted of the active electrode and a lithium metallic counter and reference electrode separated by a Celgard separator. The electrolyte used was a 0.4M solution of high quality LiTfDI in EC:DEC (1:1 ratio by volume) the latter purchased from Aldrich. Both solvents and salt were used as received. The samples were charged and discharged at room temperature in galvanostatic mode between 2.0V and 4.8V ($\text{Li}_2\text{FeSiO}_4$) and 2.0V and 4.0V

($\text{Li}_{2.2}\text{Fe}_{0.9}\text{SiO}_4$), with a $\sim 13\text{mA g}^{-1}$ current reflecting a C-rate of about C/25 based on complete lithium extraction/insertion using a MACCOR Series 2000 battery cyler (Figure 2).

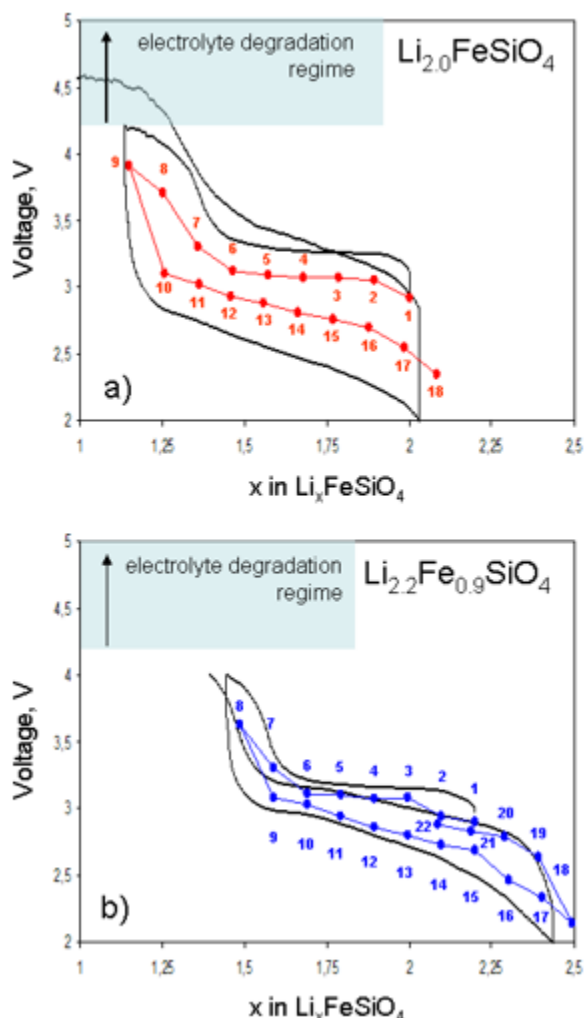


Figure 3. Calculated Li content for a) $\text{Li}_2\text{FeSiO}_4$ and b) $\text{Li}_{2.2}\text{Fe}_{0.9}\text{SiO}_4$. The black curves refer to galvanostatic charging and discharging of $1/2$ cycle, whereas the colored curves show the data of the cells used for the *in-situ* XAS experiments. The labels mentioned here are used for referring to the XAS data shown in the other figures.

The calculations of the amount of lithium extracted and inserted during battery cycling were based on the applied current and elapsed time of the charge and discharge and are plotted against the voltage. The extraction and insertion of lithium is governed by extraction and insertion electrons, thereby changing the valence of the transition metal ion. The latter being extracted from the XANES data below. Based on the model that lithium extraction above 4.2V is associated with electrolyte degradation (as opposed to further extraction of Li-ion from the material) the capacity for the electrolyte degradation has been subtracted, to predict not much lithium is extracted above 4.2V. The data of the calculated lithium contents in the samples are shown in Figure 3. The different states of charge/discharge processes are labeled 1-18 for the $\text{Li}_2\text{FeSiO}_4$ sample and 1-22 for the $\text{Li}_{2.2}\text{Fe}_{0.9}\text{SiO}_4$ sample. For both samples, the results of two cells will be shown here. More cells were analyzed, but they gave the same results (see Supplementary Information).

We note that the polarisation of $\text{Li}_{2.0}\text{FeSiO}_4$ is higher than that of $\text{Li}_{2.2}\text{Fe}_{0.9}\text{SiO}_4$, but a clear explanation of that has not been found. One possibility is the formation of a solid-electrolyte interface (SEI), leading to an increased impedance of the cell and hence the polarisation. Nevertheless, the polarisation of $\text{Li}_{2.2}\text{Fe}_{0.9}\text{SiO}_4$ is similar to that observed by Deng et al.³⁰⁻³². They also reported a reduction in the polarisation upon doping with Zn^{2+} , Cu^{2+} or Ni^{2+} . Clearly, in our case we can see $\text{Li}_{2.2}\text{Fe}_{0.9}\text{SiO}_4$ as a lithium doped $\text{Li}_{2.0}\text{FeSiO}_4$ as we replaced iron for lithium.

In situ X-Ray Absorption Spectroscopy

Data acquisition was carried out on BM26 (DUBBLE) EXAFS beamline at the European Synchrotron Radiation Facility (ESRF).³³ Spectra were collected at the Fe K-edge in transmission geometry at room temperature. The beam energy is tuned using a Si(111) double crystal monochromator, which gives an energy resolution of 1.2eV, and was calibrated using an Fe metal foil (setting the first inflection point equal to 7112 eV). The X-ray intensities are detected in ion chambers with 10% absorption in I_0 and 70% absorption in I . Data collection was made with 5eV steps through the pre-edge (7013-7093eV) regime which was shortened to 0.25eV steps while passing through the absorption edge (7094-7146eV) for the XANES measurements. The EXAFS were measured with a k space interval of 0.05\AA^{-1} between 7146 and 7610eV, corresponding to $k_{\text{min}}=3$ and $k_{\text{max}}=12\text{\AA}^{-1}$.

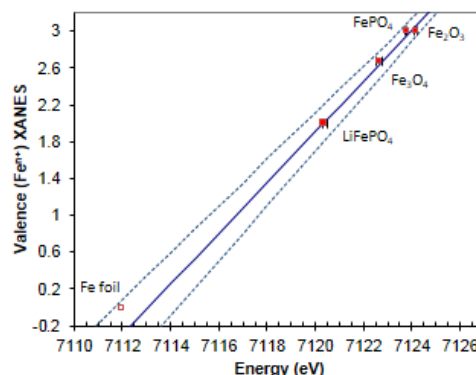


Figure 4. XANES calibration curve indicating position of the absorption edge at half height $E_{1/2}$ for standards; Fe foil, LiFePO_4 , FePO_4 , Fe_3O_4 and $\gamma\text{-Fe}_2\text{O}_3$. The standards used for calibration are represented by solid squares while the open squares (Fe foil) are included for comparison.

XAFS Data analysis

To determine the valence state of the materials the position of the absorption edge at half height $E_{1/2}$ were measured for a number of standards, *i.e.* LiFePO_4 , Fe_3O_4 , FePO_4 and $\gamma\text{-Fe}_2\text{O}_3$ (Figure 4) with varying valence state on the Fe-ions. For comparison the position of the Fe-foil is included in the graph but not included in the calibration curve regarding the valence states.

For EXAFS the absorbance ($\mu(E) = \ln\left(\frac{I_0}{I(E)}\right)$) as a function of X-ray energy (E) was analyzed using VIPER³⁴ by fitting the pre- and post-edge backgrounds to obtain $\chi(k)$ where k is the modulus of the wave vector of the photoelectron.³⁴ The EXAFS spectra give information about bond lengths and coordination numbers. Structural parameters were refined using a least squares fitting routine in EXCURVE9.27³⁵ whereby the single scattering fast curved wave theory was used to model the data. The key parameters

in the model are R_i , N_i and $2\sigma^2$, which correspond to the radial distance, the number of coordinating atoms and the Debye-Waller (DW) factor (due to static and thermal disorder) for the i^{th} shell of the neighboring atoms, respectively. The additional parameters in the model were calculated *ab initio* and are: $f(k,R)$, the backscattering amplitude of the scatterer; $2\delta(k)$, the phase shift due to the absorbing atom potential; $\Phi_i(k,R)$, the phase shift due to the scatterer; $\lambda(k)$, the inelastic mean free path of the photoelectron. Lastly, the parameter $S_0^2(k)$, the amplitude reduction factor due to many electron processes, was estimated to be equal to 0.64 by fitting to reference samples of Fe_3O_4 and $\gamma\text{-Fe}_2\text{O}_3$. Refinement was conducted on k^3 weighted data until R_f , the goodness of fit factor was minimized. This resulted in good fits for the entire k range with R_f factors less than 30% for the majority of data. The expected errors in R are ± 0.02 and in DW factor $\pm 20\%$

For the EXAFS measurements, both $\text{Li}_2\text{FeSiO}_4$ and $\text{Li}_{2.2}\text{Fe}_{0.9}\text{SiO}_4$, have been fitted with a structural model consisting of four oxygen atoms around the central Fe cation at an initial distance of 1.96 Å. This is followed by a secondary shell of four silicon at a starting distance of 3.15 Å, and a further oxygen shell at 3.49 Å. This model is based on analyses of the crystal structures reported for *pristine*, *delithiated*, and *cycled* $\text{Li}_2\text{FeSiO}_4$ (Table 1). In fitting this model to the experimental EXAFS, the neighboring Li atoms are disregarded due to their negligible effect on the photoelectron scattering. Refinement of the data was performed by allowing several parameters to vary: E_F (the Fermi energy, relative to E_0 edge position), R , DW, while the coordination number (N) and amplitude reduction factor ($S_0^2(k)$) were held fixed.

$\text{Li}_x\text{FeSiO}_4$	Shell	$R(\text{Å})$	N
Pristine $\text{P}2_1/n (\gamma)^5$	O	2.04	4
	Si	3.12	4
	O	3.49	7
Delithiated $\text{P}mn2_1 (i-\beta_{II})^{15}$	O	1.90	4
	Si	3.11	4
	O	3.53	7
Cycled $\text{P}mn2_1 (\beta_{II})^{15}$	O	2.01	4
	Si	3.12	4
	O	3.47	7

Table 1 A summary of structural parameters for Fe sites in the *pristine*, *delithiated* and *cycled* $\text{Li}_2\text{FeSiO}_4$ from crystal structures reported in the literature. Debye Waller refers to static disorder in this instance.

Results and Discussion

Valence State during battery cycling

The galvanostatic curves as a function of time are plotted in Figure 2. In both samples a voltage plateau is observed at approximately 3.2V. In the case of $\text{Li}_2\text{FeSiO}_4$ a second plateau is distinguished at about 4.3V. The 4.3V plateau for the $\text{Li}_{2.2}\text{Fe}_{0.9}\text{SiO}_4$ sample is not reported here, but has been recorded in other cells. It has been considered in the literature that the high voltage plateau appearing beyond 4V is related either to the $\text{Fe}^{3+}/\text{Fe}^{4+}$ redox couple or to electrolyte degradation rather than lithium extraction from the host material as indicated in Figure 2 by the blue shaded area.

To determine if it is possible to access the $\text{Fe}^{3+}/\text{Fe}^{4+}$ redox pair with the current battery design XANES spectra for the two samples, $\text{Li}_2\text{FeSiO}_4$ and $\text{Li}_{2.2}\text{Fe}_{0.9}\text{SiO}_4$, during the first two charging cycles were recorded. The bottom right insets in Figure 5 clearly show the change in half-height position of the main absorption edge during the first cycle, which is due to the change in valence of Fe.

First Battery cycle

The oxidation states of Fe are shown in Figure 6 in relation to the degree of delithiation. In the case of *pristine* $\text{Li}_2\text{FeSiO}_4$, the estimated valence is $\text{Fe}^{+2.10}$. It may differ from exactly +2 due to the small amount of Fe^{+3} impurities inherent in the synthesized material. However, it is evident that removal of lithium causes an increase in the valence of Fe from $\text{Fe}^{+2.10}$ to $\text{Fe}^{+2.95}$, after charging to 3.9V. Upon reinsertion of lithium the valence decreases until Fe reaches the original value of approximately +2.10. Further insertion of lithium reduces the valence of Fe to the value of +1.95. At this point more lithium has been inserted than removed. In real batteries this would be a purely hypothetical situation because the amount of lithium in the system is defined by the contents of the cathode, rather than a steady supply from a lithium anode. (It is also important to keep in mind the error bars of the XANES data).

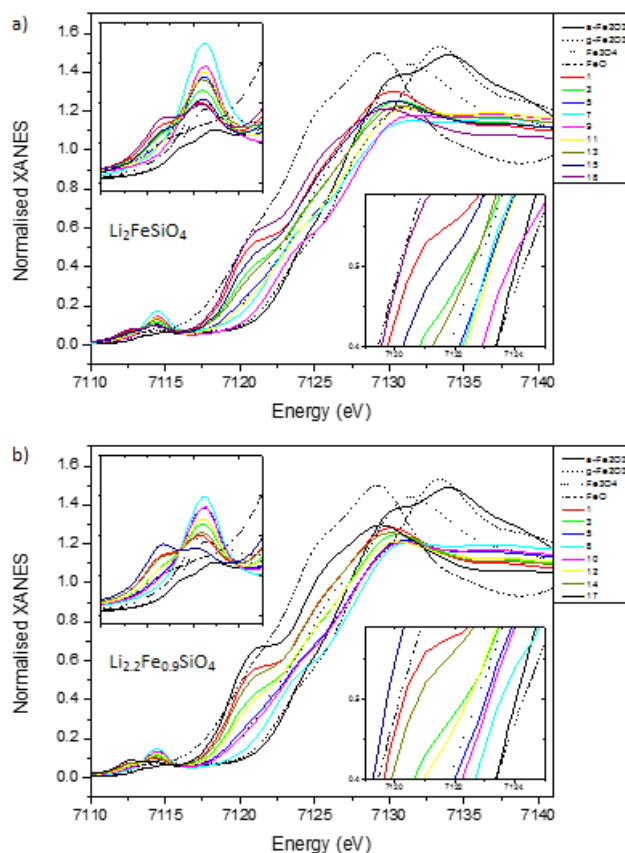


Figure 5. *In situ* XANES data for samples at various points of charge and discharge for a) $\text{Li}_2\text{FeSiO}_4$ and b) $\text{Li}_{2.2}\text{Fe}_{0.9}\text{SiO}_4$. Top left: pre-edge. Central: normalized XANES. Bottom right: edge position at half height $E_{1/2}$. Spectra of standard materials are included as reference.

The as prepared $\text{Li}_{2.2}\text{Fe}_{0.9}\text{SiO}_4$ material has an estimated valence state approaching $\text{Fe}^{+2.00}$. This increases to $\text{Fe}^{+2.85}$ upon charging to 4V and is further reduced to $\text{Fe}^{+2.15}$ by inserting the same amount of lithium. Attempts to insert more lithium led to a further decrease in valence to $\text{Fe}^{+1.85}$.

Second Battery cycle

The XANES measurements during charging to 4.8V do not show any evidence of Fe valence state higher than +3, and hence no evidence for the occurrence of Fe^{+4} . As a result, the observed plateau around 4.3V could be associated with electrolyte degradation. However, we note that several groups reported capacities higher than were theoretically predicted when charging beyond 4.2V. Some groups have inferred this to the oxidation of Fe^{+3} to the Fe^{+4} valence state,⁶ rather than electrolyte degradation and associated parasitic reactions. One difference in this battery design is the choice of salt, which will affect electrolyte reactions, and possibly the lifetime of the Fe^{+4} species, which might be very short lived. We recognise that our cells have been allowed to relax (to *circa* 4V) prior to XAS measurement, while the cells by Lv et al.⁶ were measured during cycling.

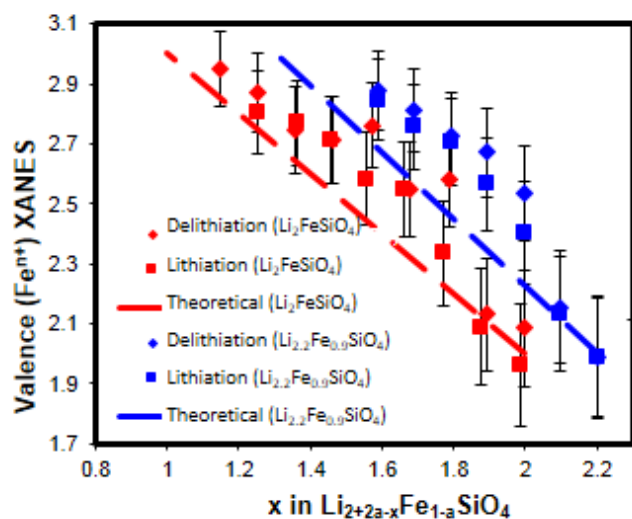


Figure 6: Amount of lithium (from electrochemistry) vs valence (from XANES data). The dashed red and blue lines indicate a theoretical value of Fe valence, during lithiation/delithiation for $\text{Li}_2\text{FeSiO}_4$ and $\text{Li}_{2.2}\text{Fe}_{0.9}\text{SiO}_4$ respectively.

On the discharge, *i.e.* insertion of lithium, all the cells show that more lithium can be accepted than was extracted, irrespective if the cells were charged above 4V or not. This then would suggest a lower Fe valence than of +2, but this is not supported by the XANES data (see section 3.2). Instead, it is suggested that the initial samples were slightly oxidized *i.e.* the Fe valence was originally higher than +2. A higher Fe valence leads to less Li extraction on the charge. However, on the discharge, all available Fe^{+3} is allowed to be reduced, and since there is more Fe^{+3} than there was initial Fe^{+2} , more lithium can be inserted after the first charge cycle. This higher valence of the initial Fe in $\text{Li}_2\text{FeSiO}_4$ or $\text{Li}_{2.2}\text{Fe}_{0.9}\text{SiO}_4$ has been reported earlier by Lv et al.⁶ This Fe^{+3} arises from the air oxidation of the nanoparticulate $\text{Li}_2\text{FeSiO}_4$ and $\text{Li}_{2.2}\text{Fe}_{0.9}\text{SiO}_4$ material. This air oxidation occurs both during transfer of the as-synthesised material

to the glovebox and, in this instance, during the electrode preparation for the *in situ* measurements

It is clear from these results that the two samples behave similarly after the first charge cycle, provided we have a lithium source at the negative electrode. Hence, we do not have any indication of stabilisation in the case of the $\text{Li}_{2.2}\text{Fe}_{0.9}\text{SiO}_4$ sample. It is further stressed that once the material is being used in a cell without a Li source, such as with carbonaceous negative electrodes, these $\text{Li}_{2+2a}\text{Fe}_{1-a}\text{SiO}_4$ materials need to be made impurity free.

Local structure

Coordination numbers

In Figure 5 the top left insets show the details of the pre-edge peaks of the XANES spectra. The *pristine* $\text{Li}_2\text{FeSiO}_4$ sample displays two distinct peaks in the pre-edge region of the spectra. The peaks correspond to Fe^{2+} in a tetrahedral environment.³⁶ As lithium is removed from the cathode Fe^{+2} is oxidised to Fe^{+3} giving rise to a singular pre-edge feature, corresponding to Fe^{+3} in a tetrahedral environment.³⁷ Upon re-insertion of Li the two peaks, characteristic of Fe^{+2} in the tetrahedral environment, re-appear again in the pre-edge spectra.

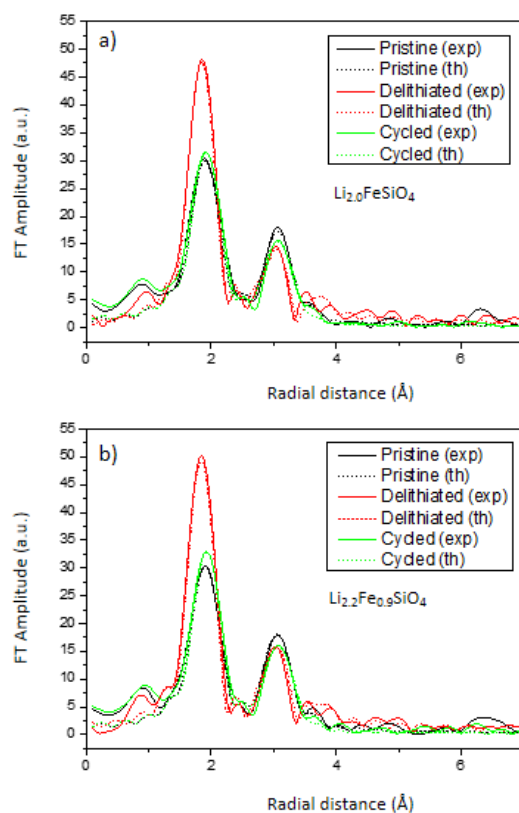


Figure 7: Radial distribution functions by Fourier Transform of k^3 weighted Fe EXAFS spectra (calculated in the k range of 3.0 to 12 \AA^{-1}) for *pristine*, *delithiated* and *cycled* structures. a) $\text{Li}_2\text{FeSiO}_4$ b) $\text{Li}_{2.2}\text{Fe}_{0.9}\text{SiO}_4$. The best fit parameters for the EXAFS are given in Table 2.

Bond Lengths

Figure 7 shows the Fourier transform (FT) of the EXAFS spectrum for the two samples at different stages during the first charging cycle. There are no reports in the literature for crystal

structures of $\text{Li}_{2.2}\text{Fe}_{0.9}\text{SiO}_4$ so the same approach to EXAFS analysis has been used for both $\text{Li}_2\text{FeSiO}_4$ and $\text{Li}_{2.2}\text{Fe}_{0.9}\text{SiO}_4$ samples.

Considering the two as prepared samples there is a prominent peak in both spectra, corresponding to the first shell of Fe-O bonds at approximately 2\AA . A second prominent peak is observed at approximately 3.5\AA associated with the Fe-Si neighbours and a second Fe-O shell. Table 2 shows the fitted results for the two samples.

The radial distribution functions shown in Figure 7 for both samples show reversible differences in both amplitude and bond length of the first shell (Fe-O) as the sample is charged and then discharged. The changes in bond length of the first shell (Fe-O) are shown in Figure 8. Combining the estimated valence from the XANES measurements with the fitted value of Fe-O bond lengths presents a linear, inverse relationship. As expected when Fe is located in a tetrahedral environment with a variable valence state of Fe^{+2} to Fe^{+3} .

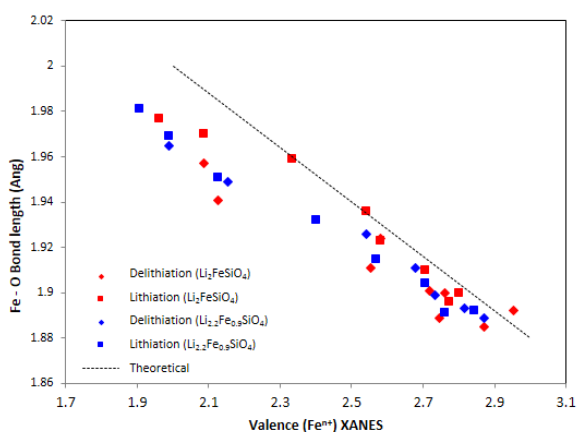


Figure 8. Valence vs Fe-O bond-length for both $\text{Li}_2\text{FeSiO}_4$ (red markers) and $\text{Li}_{2.2}\text{Fe}_{0.9}\text{SiO}_4$ (blue markers) in the first cycle. Delithiation and lithiation of the material is indicated by diamonds and squares respectively. The dashed line represents a theoretical Fe-O bond-length for Fe changing between +2 and +3 valence state.³⁴

The *pristine* $\text{Li}_2\text{FeSiO}_4$ sample has an estimated valence of +2.10, in a tetrahedral environment with a bond length of 1.96\AA in fair comparison with the literature, which reports results for Fe^{+2} in a tetrahedral environment with a typical bond length of 2.00\AA .³³ This compares with Sirisopanaporn et al²¹ who reported the γ structure to have a Fe-O bond length of 2.03\AA while a similar theoretical value of 2.05\AA was reported by Eames and coworkers.¹⁴

Upon delithiation of the $\text{Li}_2\text{FeSiO}_4$ sample the estimated valence increases to +2.95 with an associated shortened bond length to 1.89\AA , which is again consistent with the literature that reports a Fe-O distance of 1.88\AA for Fe^{+3} in a tetrahedral environment. Computations by Eames *et al.* on the *inverse beta* polymorph give a value of 1.92\AA .¹⁴ It is evident that removing lithium from the sample causes an increase in valence and subsequent contraction of the Fe-O bond. As lithium is re-intercalated into the bulk of the cathode the estimated valence returns to +2.10 with an associated Fe-O bond length of 1.96\AA . Then there is further re-insertion of Li which leads to a slightly lower valence of +1.95, seen as an additional lengthening of the Fe-O distance to 1.98\AA . This is good agreement with Armstrong et al (2.03\AA) and Eames et al (2.05\AA) for the *beta* cycled structure.^{5,14}

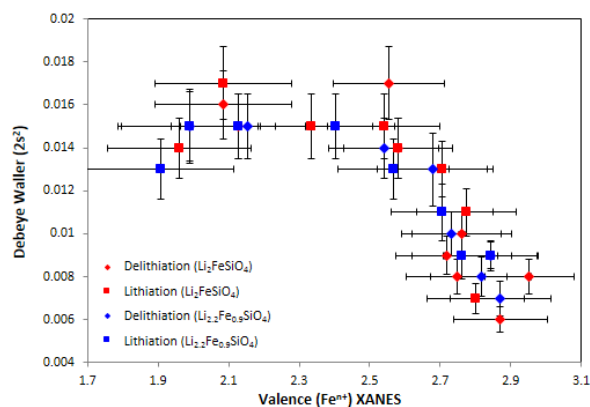


Figure 9. Valence vs Fe-O Debye Waller factor for $\text{Li}_2\text{FeSiO}_4$ (red markers) and $\text{Li}_{2.2}\text{Fe}_{0.9}\text{SiO}_4$ (blue markers) during the first cycle. Delithiation and lithiation of the material is indicated by diamonds and squares, respectively.

The information obtained from fitting the first Fe-O shell includes relationship of the Debye Waller factor to valence state. It is evident from Figure 9 that the Debye Waller factor is high in the *pristine* material indicative of a distorted FeO_4 tetrahedral site. As the cathode undergoes charging, the DW factor increases slightly due to the mixed sites of Fe^{+2} and Fe^{+3} with different bond lengths. As the valence increases to approximately $\text{Fe}^{+2.6}$ the DW factor starts to decrease. This infers an increased proportion of Fe^{+3} having a narrower range in Fe-O bond lengths in accordance with more regular FeO_4 tetrahedra. Eames *et al.*¹⁴ suggests that upon delithiation the distortion of the FeO_4 tetrahedra is reduced and the reduction in the Fe-O Debye Waller factor from the EXAFS analysis is consistent with this.

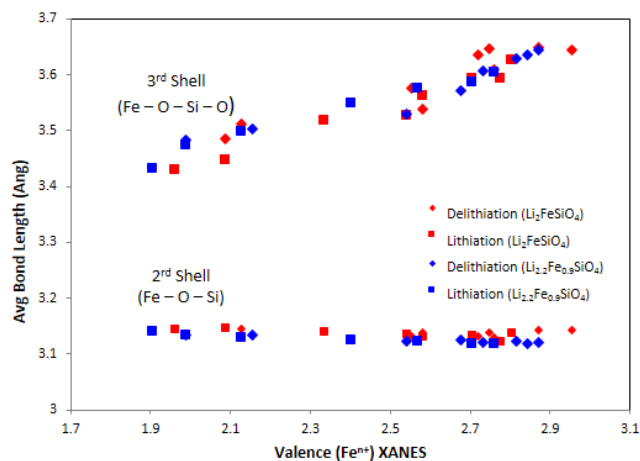


Figure 10. Valence vs Bond distance for both the 2nd shell (Fe-Si) and 3rd shell (Fe-O) in the first cycle for $\text{Li}_2\text{FeSiO}_4$ and $\text{Li}_{2.2}\text{Fe}_{0.9}\text{SiO}_4$. Delithiation and lithiation of the material is indicated by diamonds and squares respectively.

By analyzing the remaining shells it is possible to relate the local structural changes to the reported crystal structures for *pristine*, *delithiated*, and *cycled* materials. Figure 10 illustrates the variation in distances for the second and third shells. For both $\text{Li}_2\text{FeSiO}_4$ and $\text{Li}_{2.2}\text{Fe}_{0.9}\text{SiO}_4$ samples the second shell (Fe-Si) does not exhibit

discernible changes in amplitude or peak position while the third shell (Fe-O) shows increased amplitude and shifts to longer distance upon cycling. It indicates that the Fe-Si distance is relatively unchanged upon cycling, which is consistent with literature reports in Table 1. The Fe-Si distance in the *pristine* material is 3.15 Å in good comparison with 3.12 Å reported by Eames *et al.*¹⁴ Delithiation of the material does not change the Fe-Si distance of 3.15 Å. This agrees with the predictions regarding the *delithiated inverse β* structure where a Fe-Si distance of 3.11 Å is reported.¹⁴ The strength of the Fe-O-Si connection provides the material with its thermal stability and therefore enhanced safety attributes. Note that the Fe-Si distance corresponds to Fe-O-Si connected tetrahedra, where Si-O is constant and Fe-O contracts during delithiation, but the relative orientation of the tetrahedra change to keep the Fe-Si distance approximately constant. This can be explained by a competitive tradeoff between the attractive forces of Fe-O and the cation-cation repulsion between Fe⁺³ and Si⁺⁴, which results in the Fe-O-Si bond angle increasing.¹⁴

Li _x FeSiO ₄	Shell	R(Å)	N	DW factor 2σ ² (Å ²)	R _f (%)
Point 1 P ₂ /n (γ _s) Pristine	O	1.96 (1)	4	0.016 (1)	30
	Si	3.15 (1)	4	0.019 (3)	
	O	3.49 (4)	7	0.038 (9)	
Point 9 Pmn ₂ (i-β _{II}) Delithiated	O	1.89 (3)	4	0.008 (1)	18
	Si	3.14 (9)	4	0.023 (3)	
	O	3.65 (3)	7	0.036 (8)	
Point 18 Pmn ₂ (β _{II}) Cycled	O	1.98 (1)	4	0.014 (1)	31
	Si	3.15 (2)	4	0.021 (6)	
	O	3.43 (5)	7	0.067 (9)	

Li _x Fe _{0.9} SiO ₄	Shell	R(Å)	N	DW Factor 2σ ² (Å ²)	R _f (%)
Point 1 P ₂ /n (γ _s) Pristine	O	1.97 (1)	4	0.015 (1)	30
	Si	3.13 (1)	4	0.018 (3)	
	O	3.48 (4)	7	0.042 (9)	
Point 8 Pmn ₂ (i-β _{II}) Delithiated	O	1.89 (1)	4	0.007 (1)	15
	Si	3.12 (1)	4	0.019 (2)	
	O	3.64 (2)	7	0.033 (8)	
Point 17 Pmn ₂ (β _{II}) Cycled	O	1.98 (1)	4	0.013 (1)	31
	Si	3.14 (2)	4	0.021 (4)	
	O	3.43 (6)	7	0.059 (9)	

Table 2. Structural parameters for Li₂FeSiO₄ and Li_{2.2}Fe_{0.9}SiO₄ at states of charge associated with the *pristine*, *delithiated* and *cycled* materials – corresponding to points in Figure 2. The coordination number (N) remained fixed while the distance (R) and Debye Waller (2σ²) were free to vary until the R_f was minimized. Uncertainty of the last digit is given in parentheses.

Figure 10 shows that the third shell Fe-O distance gets longer approximately linearly with change in valence. The distances obtained from EXAFS fitting increase in length from 3.40 Å to 3.65 Å from *pristine* to *delithiated* material. The same trend of lengthening the Fe-O distance in the 3rd shell is seen in the reported crystal structures in Table 1, from Armstrong (*pristine*) and Eames *et al.* (*delithiated* and *cycled*).^{5,14} The increase in the Fe-O distance, corresponding to the third shell, arises from Fe-O-Si-O linkages and increases due to the increase in the Fe-O-Si bond angle as discussed previously.

Conclusions

Detailed *in situ* Fe K-edge XANES and EXAFS results have been presented for highly pure samples of Li₂FeSiO₄ and Li_{2.2}Fe_{0.9}SiO₄ cathode materials.

- Analysis of the *in situ* XANES data shows that the Fe valence remains between Fe⁺² and Fe⁺³, while Fe⁺⁴ was not evident in this voltage regime. Instead, we attribute any additional capacity to electrolyte degradation at voltages above 4.2V in this study.
- Air oxidation of the sample during electrode preparation accounts for the substantial difference between charge and discharge capacities during the first electrochemical cycle. Therefore, more lithium can be inserted upon discharging, than can be removed during charging.

In situ Fe K-edge EXAFS data have been analysed to include details of the first three neighbouring shells, Fe-O, Fe-Si and Fe-O. These data obtained during the first cycle with charging to 4.8V provide an important experimental comparison for the structural models of *pristine*, *delithiated* and *cycled* Li₂FeSiO₄ which have been reported in the literature.

- The quantitative Fe valence estimates from XANES, and the Fe-O bond length from EXAFS are both consistent with the cycling of valence state from Fe⁺² to Fe⁺³ in the reported structures. The first shell Fe-O DW factor, the second shell Fe-Si, and the third shell Fe-O distances also change according to previously reported structural models.
- The constant Fe-Si distance, despite changes to the environment of the FeO₄ tetrahedra, underlines the stability of the Li₂FeSiO₄ material, and hence its desirability in battery applications from a safety point.

This study has also presented the first results for the closely related Li_{2.2}Fe_{0.9}SiO₄ cathode material. All of the above observations also apply to this material suggesting that changing the stoichiometry in this manner does not provide any additional structural stability.

Acknowledgements

The authors are members of ALISTORE-ERI. The financial support (for AB) from ALISTORE-ERI is thankfully acknowledged. The authors would like to acknowledge the DUBBLE beamline staff for useful discussions and first class support. The Netherlands Organization for Scientific Research is also thanked for access to the DUBBLE beam lines.

Notes and references

^a School of Physical Sciences, University of Kent, Canterbury, CT2 7NH, UK.

^b Netherlands Organisation for Scientific Research (NWO), DUBBLE CRG@ESRF Grenoble 38042, France

^c School of Chemistry, University of St Andrews, Fife KY16 9ST, St Andrews, UK

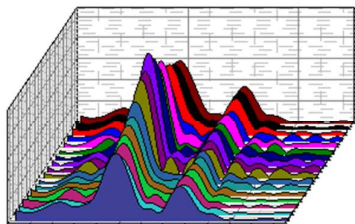
^d Laboratory for Materials Electrochemistry, NIC, Hajdrihova 19, SI-1000, Ljubljana, Slovenia

^e Delft University of Technology, Chemical Engineering, Julianalaan 136, 2628 BL, Delft, Netherlands

† corresponding author: m.l.alfredsson@kent.ac.uk

- 1 N.S Choi, Z. Chen, S. A. Freunberger, X. Ji, Y.K.Sun, K. Amine, G. Yushin, L.F. Nazar, J. Cho, P.G. Bruce, *Angew Chem Int Ed Engl.* 2012, **51**, 9994.
- 2 P.G. Bruce, B. Scrosati, J.-M. Tarascon, *Angew Chem Int Ed*, 2008, **47**, 2930.
- 3 J.B. Goodenough, Y. Kim, *Journal of Power Sources* 2011, **196**, 6688.
- 4 M.S. Islam, R. Dominko, C. Masquelier, C. Sirisopanaporn, A.R. Armstrong, P.G. Bruce, *J. of Mat. Chem.* 2011, **21**, 9811.
- 5 A.R. Armstrong, N. Kuganathan, M.S. Islam, P.G Bruce, *J. of the Am. Chem. Soc.*, 2011, **133**, 13031.
- 6 D. Lv, J. Bai, P. Zhang, S. Wu, Y. Li, W. Wen, Z. Jiang, J. Mi, Z. Zhu, Y. Yang, *Chem. of Mater.*, 2013, **25**, 2014.
- 7 A. Kokalj, R. Dominko, G. Mali, A. Meden, M. Gaberscek, J. Jamnik, *Chem. of Mater.*, 2007, **19**, 3633.
- 8 D. Lv, W. Wen, X. Huang, J. Bai, J. Mi, S. Wu, Y. Yang, *J. of Mater. Chem.*, 2011, **21**, 9506.
- 9 A.R. Armstrong, C. Lyness, M. Ménétrier, P.G. Bruce, *Chem. of Mater.*, 2010, **22**, 1892.
- 10 A. Boulineau, C. Sirisopanaporn, R. Dominko, A.R. Armstrong, P.G. Bruce, C. Masquelier, *Dalton Trans.*, 2010, **39**, 6310.
- 11 C. Sirisopanaporn, A. Boulineau, D. Hanzel, R. Dominko, B. Budic, A.R. Armstrong, P.G. Bruce, C. Masquelier, *Inorg. Chem.*, 2010, **49**, 7446.
- 12 C. Sirisopanaporn, R. Dominko, C. Masquelier, A.R. Armstrong, G. Mali, P.G. Bruce, *J. of Mater. Chem.*, 2011, **21**, 17823.
- 13 A. Nyttén, A. Abouimrane, M. Armand, T. Gustafsson, J.O. Thomas, *Electrochem. Comm.* 2005, **7**, 156.
- 14 C. Eames, A.R. Armstrong, P.G. Bruce, M.S. Islam, *Chem. of Mater.*, 2012, **24**, 2155.
- 15 D.W. Su, H.J Ahn, G.X. Wang, *Appl. Phys. Lett.*, 2011, **99**.
- 16 S.Q. Wu, Z.Z. Zhu, Y. Yang, Z.F. Hou, *Comput. Mater. Sci.*, 2009, **44**, 1243.
- 17 P. Larsson, R. Ahuja, A. Nyttén, J.O. Thomas, *Electrochem. Comm.*, 2006, **8**, 797.
- 18 A. Liivat, J.O. Thomas, *Solid State Ionics*, 2011, **192**, 58.
- 19 A. Saracibar, A. Van der Ven, M.E. Arroyo-de Dompablo, *Chem. of Mater.*, 2012, **24**, 495.
- 20 M.E. Arroyo-de Dompablo, M. Armand, J.M. Tarascon, U. Amador, *Electrochem. Comm.*, 2006, **8**, 1292.
- 21 G. Zhong, Y. Li, P. Yan, Z. Liu, M. Xie, H. Lin, *J. of Phys. Chem. C*, 2010, **114**, 3693.
- 22 R. Dominko, M. Bele, M. Gaberšček, A. Meden, M. Remškar, J. Jamnik, *Electrochem. Comm.*, 2006, **8**, 217.
- 23 C. Sirisopanaporn, C. Masquelier, P.G. Bruce, A.R. Armstrong, R. Dominko, *J. of Am. Chem. Soc.*, 2010, **133**, 1263.
- 24 R. Dominko, I. Arčon, A. Kodre, D. Hanžel, M. Gaberšček, *J. of Power Sourc.*, 2009, **189**, 51.
- 25 S. Zhang, C. Deng, S. Yang, *Electrochem. and Solid-State Lett.*, 2009, **12**, A136.
- 26 P. Zuo, T. Wang, G. Cheng, C. Du, Y. Ma, X. Cheng, G. Yin, *J. of Solid State Electrochem.*, 2013, **17**, 1955.
- 27 Y.-X. Li, Z.-L. Gong, Y. Yang, *J. of Power Sources*, 2007, **174**, 528.
- 28 T. Kojima, A. Kojima, T. Miyuki, Y. Okuyama, T. Sakai, *J. of Electrochem. Soc.*, 2011, **158**, A1340.
- 29 K.C. Kam, T. Gustafsson, J.O. Thomas, *Solid State Ionics*, 2011, **192**, 356.
- 30 C. Deng, S. Zhang, S.Y. Yang, B.L. Fu, L. Ma, *J.Power Sources*, 2011, **196**, 386.

- 31 C. Deng, S. Zhang, B.L. Fu, S.Y. Yang, L. Ma, *Mat. Chem. Phys.*, 2010, **120**, 14.
- 32 C. Deng, S. Zhang, G.S. Zhao, Z. Dong, Y. Shang, Y.X. Wu, and B.D. Zhao, *J. Electrochem. Soc.*, 2013, **160**, A1457.
- 33 S. Nikitenko, A.M. Beale, A.M.J Van Der Eerden, S.D.M. Jacques, O. Leynaud, M.G. O'Brien, D. Detollenaere, R. Kaptein, B.M. Weckhuysen, W. Bras, *J. of Synchro. Rad.*, 2008, **15**, 632.
- 34 K. Klementiev, XANES dactyloscope - CELLS., 2013.
- 35 K. Klementiev, B.G. Searle, A. Wander, N.M. Harrison A.J. Dent J.F.W. Mosselman J.E. Inglesfield; *CCLRC Technical Report*, No. DL-TR-2005-001: Warrington, UK, 2004.
- 36 M. Wilke, G.M. Partzsch, R. Bernhardt, D. Lattard, *Chem. Geol.*, 2005, **220**, 143.
- 37 F. Farges, Y. Lefrère, S. Rossano, A. Berthereau, G. Calas, Jr. G.E. Brown Jr, , 2004, **344**, 176.



The valence and local structures of Fe during battery cycling of $\text{Li}_2\text{FeSiO}_4$ and $\text{Li}_{2.2}\text{Fe}_{0.9}\text{SiO}_4$ are studied by *in-situ* (XAS) measurements.